

Deep MAGSAC++

Wei Tong¹, Jiri Matas³, and Daniel Barath²

¹ Faculty of Informatics, Eotvos Lorand University

² Department of Computer Science, ETH Zurich

³ VRG, Faculty of Electrical Engineering, Czech Technical University in Prague
weitong@student.elte.hu, matas@cmp.felk.cvut.cz, danielbela.barath@inf.ethz.ch

Abstract. We propose Deep MAGSAC++ combining the advantages of traditional and deep robust estimators. We introduce a novel loss function that exploits the orientation and scale from partially affine covariant features, e.g., SIFT, in a geometrically justifiable manner. The new loss helps in learning higher-order information about the underlying scene geometry. Moreover, we propose a new sampler for RANSAC that always selects the sample with the highest probability of consisting only of inliers. After every unsuccessful iteration, the probabilities are updated in a principled way via a Bayesian approach. The prediction of the deep network is exploited as prior inside the sampler. Benefiting from the new loss, the proposed sampler and a number of technical advancements, Deep MAGSAC++ is superior to the state-of-the-art both in terms of accuracy and runtime on thousands of image pairs from publicly available real-world datasets for essential and fundamental matrix estimation.

Keywords: RANSAC; epipolar geometry; inlier probability prediction; sampler

1 Introduction

The RANSAC (RANDOM SAMPLE CONSENSUS) algorithm proposed by Fischler and Bolles [16] in 1981 has become the most widely used robust estimator in computer vision. RANSAC and its variants have been successfully applied in a wide range of vision applications, e.g., short baseline stereo [45,47], wide baseline matching [34,28,30], to perform [54,8] or initialize multi-model fitting algorithms [23,33], image mosaicing [19], pose-graph initialization for SfM pipelines [40,41], motion segmentation [45]. Briefly, RANSAC repeatedly selects random minimal subsets of the data points, and fits a model, e.g., a 3D plane to three points or an essential matrix to five 2D point correspondences. The quality of the model is then measured, for instance, as the cardinality of its support, i.e., the number of data points closer than a manually set inlier-outlier threshold. Finally, the model with the highest quality, polished, e.g., by least-squares fitting on all inliers, is returned.

Since the publication of RANSAC, a number of modifications have been proposed replacing components of the original algorithm. To improve the accuracy by better modelling the noise in the data, different model quality calculation techniques have been investigated. For instance, MLESAC [46] estimates the quality by a maximum likelihood procedure with all its beneficial properties. In MSAC [46], the loss is formulated

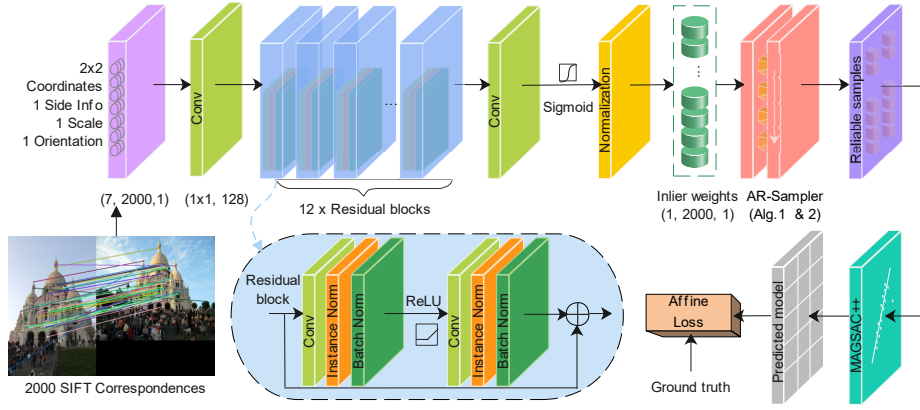


Fig. 1. **Deep MAGSAC++**. The point coordinates, SIFT orientations and scales and other information (*e.g.*, SNN ratio [25]) are fed into the network. The predicted inlier probabilities are used as prior and updated inside MAGSAC++ [9] by the proposed AR-sampler (see Section 4). The estimated model, *e.g.* relative pose, is used to calculate the loss that combines the proposed Affine Loss (see Section 3) and other widely used ones.

as a truncated quadratic error by assigning constant loss to the outliers (*i.e.*, points with residuals larger than the inlier-outlier threshold) and a quadratic one to the inliers. In the recently proposed MAGSAC++ [9], the model quality calculation is formulated as a marginalization over a range of noise scales. It allows MAGSAC++ to be significantly less sensitive to the inlier-outlier threshold than other robust estimators. According to a recent survey [26], MAGSAC++ is currently the most accurate robust estimator. In this paper, we focus on combining MAGSAC++ with deep learning improvements trained on a new loss and combined with a new sampler.

Improving the sampler accelerates the robust estimation procedure via selecting a good sample early and triggering the termination criterion. The NAPSAC [31] sampler assumes that inliers are spatially coherent and, thus, it draws samples from a hypersphere centered at the first, randomly selected, location-defining point. The GroupSAC algorithm [32] assumes that inliers are often “similar” and, thus, can be separated into groups. PROSAC [14] exploits an a priori predicted inlier probability rank of each point and starts the sampling with the most promising ones. Progressively, samples that are less likely to lead to the sought model are drawn. The sampler used in [13] assumes that we are given prior knowledge, *e.g.*, from a deep network, about the inlier probability of each point. It selects samples according to the probability assuming that it follows a categorical distribution over the discrete set of observations.

Recently, several algorithms were proposed approaching the robust relative pose estimation problem using neural networks. Context normalization networks [50] is the first paper on the topic which proposes to use PointNet (MLP) with batch normalization [22] as context mechanism. Attentive context normalization networks [43] introduces a special architectural block for the task. Deep Fundamental matrix estimation [35] uses differentiable iteratively re-weighted least-squares with predicted weights. The OANet algorithm [52] introduces several architectural blocks for the cor-

response filtering. Neural Guided RANSAC [13] uses a CNe-like architecture with a different training objective. The predicted correspondence scores are exploited inside RANSAC by using a guided sampling algorithm that helps in finding accurate models early. CLNet [53] introduces several algorithmic and architectural improvements first to remove gross outliers with iterative pruning. These techniques, in general, provide alternatives for tentative correspondence pre-filtering and weighting. However, they do not replace standard robust estimation as it is shown in [3].

This paper has three main contributions. First, we focus on combining two state-of-the-art algorithms, *i.e.*, MAGSAC++ [9] and NG-RANSAC [13], in order to improve the relative pose accuracy on a wide range of scenes. Second, we propose a way of incorporating the orientation and scale from, *e.g.*, SIFT features, in a geometrically meaningful manner directly in the loss function minimized during training. The new loss leads to more accurate results than simply using pose or epipolar errors. Third, we propose a new sampler that exploits the predicted inlier probabilities in a more effective way than [14,13]. The new sampler leads to the best results even when the SNN [25] ratio is considered as the inlier probability without using neural networks. It outperforms the widely used PROSAC sampler [14] even in this standard scenario.

2 Deep MAGSAC++

We propose a learning-based approach for robust model fitting, see Fig. 1. Even though we will describe it focusing on epipolar geometry estimation, the method is *general*.

The MAGSAC++ algorithm formulates the robust estimation problem as an iteratively re-weighted least-squares (IRLS) approach. Both the model quality calculation and inlier selection are done without making strict inlier-outlier decisions. The model parameters θ_{i+1} in the $(i+1)$ th step of the IRLS are calculated from the point-to-model residual function, $D(\theta_i, \mathbf{p})$, where \mathbf{p} is a point from the input sets, as follows:

$$\theta_{i+1} = \arg \min_{\theta} \sum_{\mathbf{p} \in \mathcal{P}} w(D(\theta_i, \mathbf{p})) D^2(\theta, \mathbf{p}), \quad (1)$$

where the weight of point \mathbf{p} is determined by marginalizing over the noise scale σ as

$$w(D(\theta_i, \mathbf{p})) = \int_0^{+\infty} \mathbf{P}(\mathbf{p} \mid \theta_i, \sigma) f(\sigma) d\sigma \quad (2)$$

and $\theta_0 = \theta$, *i.e.*, the initial model from the minimal sample.

The inlier residuals are assumed to be calculated as the sum of normally distributed squared variables (*e.g.*, re-projection error), thus having χ^2 -distribution. The noise standard deviation σ is assumed to be uniformly distributed within interval $(0, \sigma_{\max})$. The weight function defined in (2) is the marginal density of the inlier residuals as follows:

$$w(r) = \int_0^{+\infty} g(r \mid \sigma) f(\sigma) d\sigma. \quad (3)$$

Let $\tau(\sigma) = k\sigma$ be the chosen quantile of the χ -distribution. For residual $0 \leq r \leq k\sigma_{\max}$,

$$w(r) = \frac{1}{\sigma_{\max}} \int_{r/k}^{\sigma_{\max}} g(r | \sigma) d\sigma =$$

$$\frac{1}{\sigma_{\max}} C(\nu) 2^{\frac{\nu-1}{2}} \left(\Gamma\left(\frac{\nu-1}{2}, \frac{r^2}{2\sigma_{\max}^2}\right) - \Gamma\left(\frac{\nu-1}{2}, \frac{k^2}{2}\right) \right)$$

and, for $r > k\sigma_{\max}$, weight $w(r) = 0$. Function

$$\Gamma(a, x) = \int_x^{+\infty} t^{a-1} \exp\{-t\} dt$$

is the upper incomplete gamma function. Due to the design choices, weight $w(r)$ is positive and decreases on interval $[0, \tau(\sigma_{\max})]$. There is a ρ -function of an M-estimator which is minimized by IRLS using $w(r)$, and each iteration guarantees a non-increase in its loss function (chapter 9 of [27]). Consequently, it converges to a local minimum.

The IRLS in Eq.(1) where $w(r)$ is defined by (3) with $\tau(\sigma) = 3.64\sigma$ (where 3.64 is the 0.99 quantile of the χ -distribution with $\nu = 4$), is called σ -consensus++ for problems using point correspondences. Parameter σ_{\max} is a user-defined maximum noise level parameter. The σ -consensus++ algorithm is applied for fitting non-minimal samples and, also, as a post-processing to improve the output of any robust estimator.

In order to improve MAGSAC++ using recent neural network-based techniques, we adopt the Neural Guided RANSAC (NG-RANSAC) architecture [13]. The NG-RANSAC algorithm predicts the probability of each point correspondence being inlier and uses a weighted sampling approach to incorporate this information in the robust estimation procedure. Due to the neural network and the robust estimator being loosely connected in such a manner, we develop an efficient learning-based robust estimator using MAGSAC++ as the core algorithm.

While training the weights with sparse correspondences end-to-end, the inlier masks and selected samples are used to update the gradients of the neurons and generate point probabilities as weights for the consequent epochs. We use additional side information as well, namely, the scale and orientation of each SIFT feature. In the next sections, we focus on improving the network by considering new geometry-induced loss functions and, also, propose a new sampler more efficiently exploiting the predicted probabilities than the importance sampler from [13] and PROSAC proposed by Chum *et al.* [14].

3 Scale and Orientation Loss

We propose a new loss function considering that, in most of the two-view cases, we apply feature detectors that provide more information about the underlying scene geometry than simply the point coordinates. For instance, ORB [39] features contain the orientation of the image patches centered on the detected points in the two images. In addition to the feature orientation, the SIFT [25] and SURF [12] detectors return a uniform scaling parameter. Even the full affine warping of the patch can be recovered when using affine-covariant feature detectors, *e.g.*, Hessian-Affine [29] or MODS [30]. The point correspondence and the affine warp is the so-called affine correspondence [6].

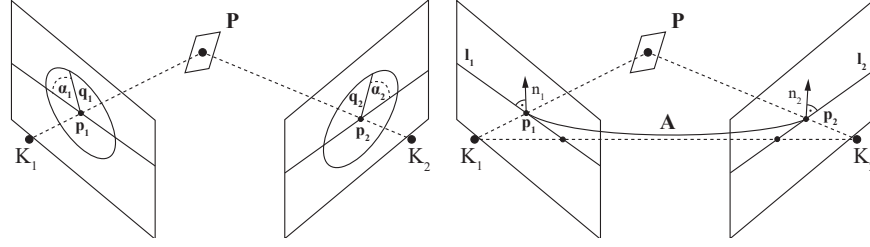


Fig. 2. **(Left)** Visualization of the orientation- and scale-covariant features. Point \mathbf{P} and the surrounding patch projected into cameras \mathbf{K}_1 and \mathbf{K}_2 . The rotation of the feature in the i th image is $\alpha_i \in [0, 2\pi)$, with size, $q_i \in \mathbb{R}$, $i \in \{1, 2\}$. **(Right)** The geometric interpretation of the relations of local affine transformations and the epipolar geometry (Eq. (4); proposed in [5]). The normal \mathbf{n}_1 of epipolar line \mathbf{l}_1 is mapped by affinity $\mathbf{A} \in \mathbb{R}^{2 \times 2}$ into the normal \mathbf{n}_2 of epipolar line \mathbf{l}_2 .

To the best of our knowledge, the additional information that such features provide has not yet been exploited in a geometrically meaningful manner to minimize the training loss. Recent deep networks, *e.g.*, [13], only use it as side information added to the learned feature vectors or for pre-filtering correspondences.

3.1 Affine Epipolar Error

In order to interpret fully or partially affine-covariant features, we adopt the definition from [5] and the affine transformation model from [4]. We consider an affine correspondence (AC) a triplet: $(\mathbf{p}_1, \mathbf{p}_2, \mathbf{A})$, where $\mathbf{p}_1 = [u_1, v_1, 1]^T$ and $\mathbf{p}_2 = [u_2, v_2, 1]^T$ are a corresponding homogeneous point pair in the two images, and

$$\mathbf{A} = \begin{bmatrix} a_1 & a_2 \\ a_3 & a_4 \end{bmatrix} = \begin{bmatrix} \cos(\alpha) & -\sin(\alpha) \\ \sin(\alpha) & \cos(\alpha) \end{bmatrix} \begin{bmatrix} q_u & w \\ 0 & q_v \end{bmatrix}, \quad (4)$$

is a 2×2 linear transformation describing the relationship of the infinitesimal image patches centered on points \mathbf{p}_1 and \mathbf{p}_2 , where α is rotation, q_u and q_v are the scales along the axes, and w is the shear parameter. Formally, \mathbf{A} is defined as the first-order Taylor-approximation of the $3D \rightarrow 2D$ projection functions. For perspective cameras, \mathbf{A} is the first-order approximation of the related 3×3 homography.

The relationship of affine correspondences and epipolar geometry is shown in [36,5], with [5] providing a geometrically interpretable definition of the constraint as

$$\mathbf{A}^{-T} \mathbf{n}_1 = -\mathbf{n}_2 \quad (5)$$

where $\mathbf{n}_1 = (\mathbf{F}^T \mathbf{p}_2)_{[1:2]}$ and $\mathbf{n}_2 = (\mathbf{F} \mathbf{p}_1)_{[1:2]}$ are the normals of the epipolar lines in the two images, and lower-index $\mathbf{v}_{[1:2]}$ selects the first two coordinates of a vector \mathbf{v} . See the right plot of Fig. 2.

While constraint (5) is originally formulated as two linear equations in [5] to simplify the estimation, it can be re-written to two geometrically meaningful constraints that we can use in the loss function. First, (5) implies that \mathbf{A}^{-T} rotates the normal in the first image to its corresponding pair in the second one as $(\mathbf{A}^{-T} \mathbf{n}_1) \times \mathbf{n}_2 = 0$, where

the angle between $\mathbf{A}^{-T}\mathbf{n}_1$ and \mathbf{n}_2 can be used as an error for an estimated fundamental matrix $\hat{\mathbf{F}}$ as follows:

$$f(\mathbf{A}, \hat{\mathbf{F}}, \mathbf{p}_1, \mathbf{p}_2) = \cos^{-1} \frac{\left(\mathbf{A}^{-T}(\hat{\mathbf{F}}^T \mathbf{p}_2)_{[1:2]} \right) (\hat{\mathbf{F}} \mathbf{p}_1)_{[1:2]}}{\left| \mathbf{A}^{-T}(\hat{\mathbf{F}}^T \mathbf{p}_2)_{[1:2]} \right| \left| (\hat{\mathbf{F}} \mathbf{p}_1)_{[1:2]} \right|}. \quad (6)$$

Second, (5) implies that the scale change is

$$\sqrt{\det \mathbf{A}} = \frac{|\mathbf{n}_2|}{|\mathbf{n}_1|} = \frac{|(\mathbf{F} \mathbf{p}_1)_{[1:2]}|}{|(\mathbf{F}^T \mathbf{p}_2)_{[1:2]}|} \quad (7)$$

providing another geometrically meaningful error as

$$g(\mathbf{A}, \hat{\mathbf{F}}, \mathbf{p}_1, \mathbf{p}_2) = \sqrt{\det \mathbf{A}} - \frac{|(\hat{\mathbf{F}} \mathbf{p}_1)_{[1:2]}|}{|(\hat{\mathbf{F}}^T \mathbf{p}_2)_{[1:2]}|}. \quad (8)$$

Overall, these errors can be used to measure the quality of a fundamental or essential matrix given an affine correspondence.

3.2 Affine Loss Function

In practice, we are usually given partially affine-covariant features, *e.g.*, SIFT, that do not allow using error functions (6) and (8) directly. In order to define a justifiable loss, we first approximate the local affine transformation $\hat{\mathbf{A}}$ using the rotations α_1, α_2 and scales q_1, q_2 from the SIFT features via the affine transformation model in (4) assuming that shear $w = 0$, rotation $\alpha = \alpha_2 - \alpha_1$, and $q_u = q_v = q_2/q_1$ is a uniform scaling along the axes similarly as in [4], see the left plot of Fig. 2. It is important to note that directly using $\hat{\mathbf{A}}$ to measure the error of the prediction is still not viable since $\hat{\mathbf{A}}$ is only an approximation and, thus, (6) and (8) are not zero even if the ground truth fundamental matrix is used. We, therefore, define our orientation loss as

$$L_{\text{ori}}(\dots) = \left| f(\hat{\mathbf{A}}, \hat{\mathbf{F}}, \mathbf{p}_1, \mathbf{p}_2) - f(\hat{\mathbf{A}}, \mathbf{F}, \mathbf{p}_1, \mathbf{p}_2) \right|,$$

and the scale loss as

$$L_{\text{scale}}(\dots) = \left| g(\hat{\mathbf{A}}, \hat{\mathbf{F}}, \mathbf{p}_1, \mathbf{p}_2) - g(\hat{\mathbf{A}}, \mathbf{F}, \mathbf{p}_1, \mathbf{p}_2) \right|,$$

where \mathbf{F} is the ground truth fundamental matrix used as a target for the network and $\hat{\mathbf{F}}$ is the prediction. Measuring the error in this way allows ignoring the approximative nature of $\hat{\mathbf{A}}$. The final loss minimized when training the network is

$$L(\mathbf{F}, \hat{\mathbf{F}}, \mathcal{P}) = \sum_{(\mathbf{p}_1, \mathbf{p}_2, \hat{\mathbf{A}}) \in \mathcal{P}} w_{\text{ori}} L_{\text{ori}}(\mathbf{F}, \hat{\mathbf{F}}, \hat{\mathbf{A}}, \mathbf{p}_1, \mathbf{p}_2) + w_{\text{scale}} L_{\text{scale}}(\mathbf{F}, \hat{\mathbf{F}}, \hat{\mathbf{A}}, \mathbf{p}_1, \mathbf{p}_2) + \dots$$

where $\mathcal{P} = \{(\mathbf{p}_1, \mathbf{p}_2, \alpha_1, \alpha_2, q_1, q_2) \mid \mathbf{p}_1, \mathbf{p}_2 \in \mathbb{R}^2 \wedge \alpha_1, \alpha_2 \in [0, 2\pi] \wedge q_1, q_2 \in \mathbb{R}^+\}$ is the set of SIFT correspondences, w_{ori} and w_{scale} are weighting parameters, and \dots represents other frequently used error metrics, *e.g.*, epipolar or pose error, or inlier number. To propagate the gradient, the training objective $L(w)$ is defined as the minimization of the expected task loss, similarly as in [13]. Since integrating over all possible hypotheses to calculate the expectation is infeasible, the gradients for the categorical distribution over the discrete set of observations are approximated by drawing K samples as

$$\frac{\partial}{\partial w} L(w) \approx \frac{1}{K} \sum_{k=1}^K [l(\hat{h}) \frac{\partial}{\partial w} \log p(H_k; w)],$$

where K is the number of samples used for approximating the gradients. The task loss is $l(\hat{h})$, and $p(H_k; w)$ denotes the learned distribution of the k th sample.

4 Adaptive Re-ordering Sampler

In this section, we describe a new sampler that always selects the sample with the highest probability of containing only inliers. This probability is updated adaptively according to the success or failure of the current minimal sample in the robust estimation procedure. The new sampler will be called **AR-Sampler** in the remainder of the paper.

Let us assume that we are given point correspondences $p_{i_1^t}, p_{i_2^t}, \dots, p_{i_n^t} \in \mathcal{P}$ with inlier probabilities $\mu_{i_1^t}, \mu_{i_2^t}, \dots, \mu_{i_n^t} \in [0, 1]$ such that $\mu_{i_1^t} \geq \mu_{i_2^t} \geq \dots \geq \mu_{i_n^t}$, where $i_1^t, \dots, i_n^t \in [1, n]$ are indices in the t th RANSAC iteration ensuring that the points are ordered by the inlier probabilities in a descending order. The probability of sample $S = (p_{j_1}, p_{j_2}, \dots, p_{j_m}) \in \mathcal{P}^\times$ consisting only of inliers is calculated as $\mu_S = \prod_{k=1}^m \mu_{j_k}$, where m is the sample size, *e.g.*, $m = 5$ for essential matrix estimation. Consequently, the optimal sampler maximizes the sample probability of $S_t^* = (p_{i_1^t}, p_{i_2^t}, \dots, p_{i_m^t})$ in the t th iteration to increase the probability of finding the sought model early.

Every unsuccessful RANSAC iteration reduces the inlier probability of the points in the minimal sample. This stems from the fact that in case of having an all-inlier sample that is good enough to find the sought model, RANSAC terminates.⁴ Otherwise, the sample is not all-inlier. Therefore, of all the possible inlier-outlier configurations in the sample, the “all points are inliers” is ruled out, and, consequently, the inlier probabilities of the sample points decrease, typically very modestly. In order to model this in a principled way, we update the probabilities using the Bayesian approach after each RANSAC iteration. We note that the Bayesian approach ignores the dependencies between points that appeared in a sample. As prior knowledge, we can either consider the output of the deep network or even the point ordering that the SNN ratio [25] implies. In each update, only the points from the current minimal sample are considered and, thus, the probability of other points remain unchanged in the $t + 1$ -th iteration as we did not gather additional information about them.

⁴ Precisely, RANSAC either terminates immediately when it finds the sought model or runs until the confidence in the result exceeds the manually set confidence threshold. In the latter case, the iterations done after finding the sought model do not change the result.

Algorithm 1 Probability Update.

Input: p_1, \dots, p_n – points; μ_1, \dots, μ_n – probabilities
 S – minimal sample; N_1, \dots, N_n – usage numbers
 $(a_1, b_1), \dots, (a_n, b_n)$ – initial distribution parameters
Output: μ'_1, \dots, μ'_n – updated inlier probabilities

```

1: for  $i \in [1, n]$  do
2:   if  $p_i \in S$  then                                 $\triangleright$  Decrease inlier probability  $\mu$  for all points in the sample
3:      $a'_i \leftarrow a_i; b'_i \leftarrow b_i + N_i$ 
4:      $\mu'_i \leftarrow a'_i / (a'_i + b'_i)$ 
5:   else                                               $\triangleright$  Other points have the same probability  $\mu$  as before
6:      $\mu'_i \leftarrow \mu_i$ 

```

Algorithm 2 Adaptive Re-ordering Sampler.

Input: p_1, \dots, p_n – points; μ_1, \dots, μ_n – inlier probs.
 m – sample size ; N_1, \dots, N_n – usage numbers
 $(a_1, b_1), \dots, (a_n, b_n)$ – initial distribution parameters
Output: S^* – minimal sample

```

1:  $i_1, \dots, i_n \leftarrow \text{sort}(\mu_1, \dots, \mu_n)$            $\triangleright$  Sort points according to the inlier probability
2:  $S^* \leftarrow \{p_{i_j} \mid j \in [1, m]\}$                  $\triangleright$  Sample the points with the highest probabilities
3: for  $p_{i_j} \in S^*$  do
4:    $N_{i_j} \leftarrow N_{i_j} + 1$                          $\triangleright$  Increase the usage number of the points in sample  $S^*$ 
5:    $\mu_{i_j} \leftarrow \text{Update}(a_{i_j}, b_{i_j}, \mu_{i_j}, N_{i_j})$   $\triangleright$  Algorithm 1

```

The probability of point \mathbf{p} being inlier in the t th iteration follows the Bernoulli distribution. Consequently, after being selected n_p times during the robust estimation, it follows the binomial distribution with parameters $\mu_p(n_p)$ and n_p . The usual conjugate prior for a binomial distribution is a beta distribution with prior hyper-parameters $a(n_p)$ and $b(n_p)$, with expectation $a(n_p)/(a(n_p) + b(n_p))$, variance

$$v = \frac{a(n_p)b(n_p)}{(a(n_p) + b(n_p))^2(a(n_p) + b(n_p) + 1)},$$

and posterior hyper-parameters $a(n_p)$ and $b(n_p)$. The posterior distribution parameters are $a(n_p + 1) = a(n_p)$, $b(n_p + 1) = b(n_p) + 1$. The best estimator for $\mu_p(n_p + 1)$ using a quadratic loss function is an expectation of the posterior distribution. Consequently,

$$\mu_p(n_p + 1) = \frac{a(n_p + 1)}{a(n_p + 1) + b(n_p + 1)}.$$

For each point \mathbf{p} , the initial parameters of the beta distribution $a(1)$ and $b(1)$ are set using the predicted inlier ratio $\mu_p(1) = \mu_p^1$. We assume that the inlier probability prediction provides the expectation of the prior beta distribution and with the same mean precision for all points. Therefore, the variance v of all these initial beta distributions is

equal and can be learned in advance. Given the learned variance, equations

$$\mu_p(1) = \frac{a(1)}{a(1) + b(1)}, \quad v = \frac{a(1)b(1)}{(a(1) + b(1))^2(a(1) + b(1) + 1)}.$$

lead to

$$a(1) = \frac{(\mu_p(1))^2(1 - \mu_p(1))}{v} - \mu_p(1), \quad b(1) = a(1) \frac{1 - \mu_p(1)}{\mu_p(1)}.$$

Parameters $a(1)$ and $b(1)$ are calculated prior to the robust estimation procedure. The sampler and the probability update are shown, respectively, in Algorithms 2 and 1. Both methods contain only a few calculations and, thus, are very efficient. This is expected from a sampler in a RANSAC-like robust estimator where it runs in every iteration, often thousands of times. Note that we found that the sampler works better if the probabilities are shuffled by adding a small random number ϵ . Setting ϵ so it is uniformly distributed in-between -0.0005 and 0.0005 works well in all our experiments.

5 Experimental Results

This section evaluates the accuracy and speed of Deep MAGSAC++ and the impact of each individual improvement proposed in this paper, *e.g.*, AR-Sampler and affine loss. The compared methods are the OpenCV RANSAC [16] and LMEDS [37], the implementations provided by the authors of GC-RANSAC [7], MAGSAC [10] and MAGSAC++ [9], NG-RANSAC [13], OANet [52] and the recently published EAS [15], and CLNet [53] algorithms. We re-trained NG-RANSAC, OANet and CLNet on the same data as used for Deep MAGSAC++. Also, we will show their results with the provided models trained on significantly more image pairs than what we use for training Deep MAGSAC++. All the experiments were conducted on Ubuntu 20.04 with GTX 3090Ti, OpenCV 4.5/3.4, and PyTorch 1.7.1.

Technical details. We use RootSIFT [2] features to improve the estimation accuracy and help the deep network to learn accurate weights. RootSIFT is a strategy normalizing the SIFT [25] descriptors, thus, helping the feature matcher to find good tentative correspondences. When training, we provide the network with the feature scales and orientations as a learned side-information. Also, we do SNN ratio [25] filtering on the correspondences as a preliminary step. In the SNN test, the correspondences are discarded if the distance between the first and the second nearest neighbors is larger than a manually set threshold, which works well as we set to 0.8 in all of our experiments.

5.1 Essential Matrix Estimation

In order to test the essential matrix estimation performance of the proposed algorithm, we downloaded the 13 scenes from the CVPR IMW 2020 PhotoTourism challenge [42]. These scenes were also used in the recent CVPR tutorial *RANSAC in 2020* [1] to compare robust estimators. The dataset contains tentative correspondences formed

by mutual nearest neighbors matching RootSIFT descriptors. It also provides SIFT orientations and scales that we can use for training the proposed method. Besides the image matches, the ground-truth intrinsic camera parameters and relative poses are also provided. We use scene St. Peter’s Square, consisting of 4950 image pairs, for training Deep MAGSAC++ and retraining NG-RANSAC, CLNet, and OANet for comparison. We use the provided validation set when training the deep learning-based algorithms. We tuned the hyper-parameters, *e.g.* inlier-outlier threshold, on the validation set. For testing, we use 1000 randomly chosen image pairs from each of the remaining 12 scenes. Thus, the methods are tested on a total of 12 000 image pairs.

Before applying the main end-to-end training, we initialize our deep model by minimizing the Kullback–Leibler divergence [49] of the prediction and the target distribution using a 1000-epoch long initial training process. To our experiments, this procedure improves the convergence speed of the end-to-end training. The end-to-end Deep MAGSAC++ framework is trained on the RootSIFT correspondences of St. Peter’s Square (4950 pairs) for 10 epochs, with its inlier-outlier threshold upper bound set to 0.75 pixels, Adam optimizer [24], a batch size of 32, and 10^{-5} learning rate are used.

In each iteration of the training, the pre-filtered correspondences are re-ordered according to the predicted weights, and MAGSAC++ with AR-Sampler is applied to estimate the essential matrix. The network can be trained both in a supervised and self-supervised manner. We report the errors of the model trained in a supervised way where the loss is a combination of the proposed affine loss (Section 3.1), and pose error. For calculating the affine loss, we used the SIFT orientation and scale and the ground truth essential matrix. The pose error is calculated as the maximum of the rotation $\epsilon_{\hat{\mathbf{R}}} = (180/\pi) \cos^{-1}((\text{tr}(\hat{\mathbf{R}}\mathbf{R}^T) - 1)/2)$, and the translation errors $\epsilon_{\hat{\mathbf{t}}} = (180/\pi) \cos^{-1} \frac{\mathbf{r}^T \hat{\mathbf{t}}}{|\mathbf{r}| |\hat{\mathbf{t}}|}$, in degrees, where $\hat{\mathbf{R}} \in \text{SO}(3)$ is the 3D rotation matrix and $\hat{\mathbf{t}} \in \mathbb{R}^3$ is the translation, both decomposed from the estimated essential matrix $\hat{\mathbf{E}}$. Note that we use the angular translation error since the length of $\hat{\mathbf{t}}$ can not be recovered from two views [20]. Also, note that the scale and orientations of the features have to be normalized together with the point correspondences by the intrinsic camera matrices \mathbf{K}_1 and \mathbf{K}_2 as proposed in [6]. While the rotation angle remains unchanged, the scale is normalized by f_2/f_1 , where f_i is the focal length of the i th camera, $i \in [1, 2]$. The network can also be trained in a self-supervised way by using the minus inlier number as the loss function maximizing the number of inliers. The proposed affine loss suits this scenario as well. However, the supervised version leads to higher accuracy in our experiments.

We adopted the neural network from [13] and [51], a typical and commonly used neural network for geometry data, which comprises 12 residual blocks that connects information from different layers and several multi-layer perceptions (MLPs). Each block is constructed by two linear layers, a batch normalization layer, and a ReLU activation function [21]. Besides, the global context is included by adding the instance normalization [48] layer into each block. The inlier probabilities of the matches are mapped by a sigmoid function. Finally, MAGSAC++ with the proposed AR-Sampler estimates the essential matrix with its iteration number fixed to 1000.

The training objective is defined as the minimization of the expected task loss, shown in [13]. We approximate the gradients for the categorical distribution over the discrete set of observations. The number of times each correspondence was selected in

Dataset / Method	LMEDS [38]	RSC [17]	GC-RSC [7]	MSC [10]	MSC++ [9]	EAS [15]	OANet [52]	CLNet [53]	NG-RSC [13]	Deep MAGSAC++
Avg. time (ms)	26.7	88.1	175.1	239.4	113.4	317.5	163.3	138.9	79.8	33.9
Buckingham Palace	0.19	0.20	0.20	0.27	0.26	0.09	0.18	0.25	0.28	0.33
Brandenburg Gate	0.34	0.42	0.48	0.53	0.54	0.29	0.48	0.54	0.55	0.61
Colosseum Exterior	0.25	0.25	0.27	0.32	0.31	0.13	0.29	0.32	0.32	0.36
Grand Place Brussels	0.14	0.14	0.17	0.22	0.21	0.06	0.18	0.22	0.22	0.32
Notre Dame Front Facade	0.24	0.27	0.38	0.40	0.41	0.13	0.32	0.37	0.34	0.49
Palace of Westminster	0.19	0.31	0.36	0.37	0.37	0.20	0.21	0.31	0.38	0.43
Pantheon Exterior	0.49	0.41	0.48	0.62	0.62	0.20	0.48	0.57	0.62	0.72
Prague Old Town Square	0.10	0.11	0.12	0.16	0.16	0.07	0.09	0.15	0.17	0.20
Sacre Coeur	0.52	0.64	0.68	0.71	0.71	0.55	0.56	0.64	0.63	0.75
Taj Mahal	0.36	0.48	0.52	0.52	0.55	0.37	0.48	0.58	0.55	0.67
Trevi Fountain	0.28	0.29	0.30	0.37	0.35	0.17	0.32	0.42	0.38	0.43
Westminster Abbey	0.46	0.36	0.49	0.51	0.51	0.20	0.38	0.44	0.49	0.70
Avg. over all scenes	0.30	0.32	0.37	0.42	0.42	0.21	0.33	0.40	0.41	0.50

Table 1. Essential matrix estimation on the PhotoTourism dataset [42]. We report the AUC scores [51] at 10° (higher is better) calculated from the pose error, *i.e.*, the max. of the relative rotation and translation errors in degrees. The first row shows the average run-times (ms). The last one reports the scores averaged over all scenes. For RANSAC, GC-RANSAC, MAGSAC and MAGSAC++, we use the threshold tuned in [11]. For EAS, the default thresholds are used. We trained OANet, CLNet, NG-RANSAC, and Deep MAGSAC++ on the same datasets. The results with the pre-trained models provided by the authors are in Table 2.

a minimal sample is back-propagated and used to update the weights and contribute to distribution learning for the next iteration.

To measure the accuracy of the estimated essential matrices, we decompose them to rotation and translation and calculate the pose error. Finally, we calculate the AUC scores at 5° , 10° and 20° from the pose errors as the area under the recall curves [13]. The AUC@ 10° scores on each scene from the PhotoTourism dataset [42] are reported in Table 1. Also, we show the run-time (in milliseconds) and the AUC scores averaged over all scenes. The proposed Deep MAGSAC++ is superior to the state-of-the-art, *i.e.* EAS, MAGSAC++, CLNet and NG-RANSAC, by a large margin both in terms of run-time and accuracy. It is the most accurate on *all* scenes. Its average score is higher by 8 AUC points than that of the second most accurate method (*i.e.*, MAGSAC++). The only method faster is LMEDS that has the second lowest accuracy.

The left plot of Fig. 3 shows the cumulative distribution functions (CDF) of the angular pose errors of the estimated essential matrices on all tested scenes. Being accurate is indicated by a curve close to the top-left corner. Deep MAGSAC++ is significantly more accurate than the other compared methods.

Furthermore, Table 2 shows the performance comparison of Deep MAGSAC++ with NG-RANSAC, CLNet and OANet when using the pre-trained models that their authors provide. CLNet and OANet was trained on 541 184 image pairs from the YFCC [44] dataset. NG-RANSAC was trained on a total of 10 000 pairs from the same scene

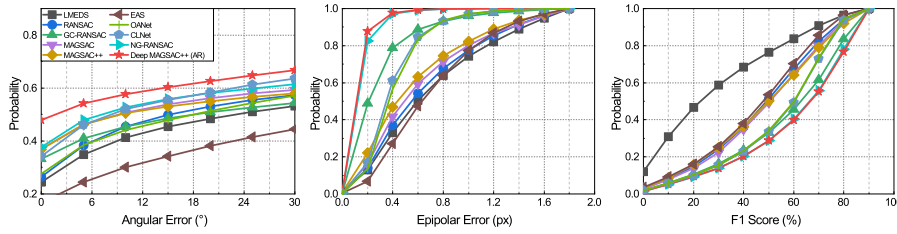


Fig. 3. The cumulative distribution functions (CDF) of the angular errors (left) for \mathbf{E} estimation; epipolar errors (middle; in pixels) and F1 score (right; in percentages) for \mathbf{F} estimation. Essential matrix estimation is tested on 12 000 image pairs from the PhotoTourism [42] dataset. Fundamental matrix estimation is tested on 9690 pairs from the KITTI [18] dataset. We use the thresholds tuned in [11] for the traditional algorithms. We trained OANet, CLNet, NG-RANSAC, and Deep MAGSAC++ on the same datasets. In the left two plots, being close to the top-left corner indicates accurate results. In the right one (F1 score), the bottom-right corner is preferable.

as what we use for Deep MAGSAC++. As a reminder, Deep MAGSAC++ was trained on 4950 image pairs in total. Even in this unfair comparison, the proposed method leads to the most accurate results in the $\text{AUC}@5^\circ$ and $\text{AUC}@10^\circ$ cases by a large margin – in the $\text{AUC}@5^\circ$ case, it is better than CLNet (*i.e.*, the second best) by 6 AUC points. This clearly shows that the Deep MAGSAC++ generalizes better than the state-of-the-art learning-based approaches and is able to learn the underlying scene geometry better thanks to the number of proposed improvements.

In the left plot of Fig. 4, we show the accuracy gained from each component of the algorithm. We show the AUC scores and their standard deviations at 5° , 10° and 20° averaged over 12 scenes. The proposed affine loss plays an important role in improved accuracy. Also, it confirms that the widely used techniques, *e.g.*, SNN filtering, RootSIFT, initial training, are important steps to achieve state-of-the-art results.

In the right plot of Fig. 4, we show the results of different samplers used within Deep MAGSAC++. The compared samplers are the uniform one from [16], the NG-RANSAC sampler [13], PROSAC [14], and the proposed AR-Sampler. It can be seen that the proposed AR-Sampler leads to the best accuracy. Interestingly, PROSAC significantly outperforms the recently proposed sampler of NG-RANSAC, which is just marginally more accurate than the uniform sampler when used inside Deep MAGSAC++.

5.2 Fundamental Matrix Estimation

We evaluate Deep MAGSAC++ for fundamental matrix estimation on the KITTI benchmark [18]. As in [51, 13], Sequences '00-05' and '06-10' are regarded as the training and testing sets, respectively. The KITTI dataset consists of consecutive frames of high-resolution cameras rigidly mounted to a moving vehicle in a mid-size city, rural areas and highways [18]. The images are of resolution 1226×370 . Image correspondences are detected between subsequent images by RootSIFT. In total, we use 14 130 image pairs from KITTI for training, and another 9060 for testing.

Fundamental matrix estimation runs on the same architecture as what we described in Section 5.1. In this case, neither the point coordinates, nor the orientation and scale

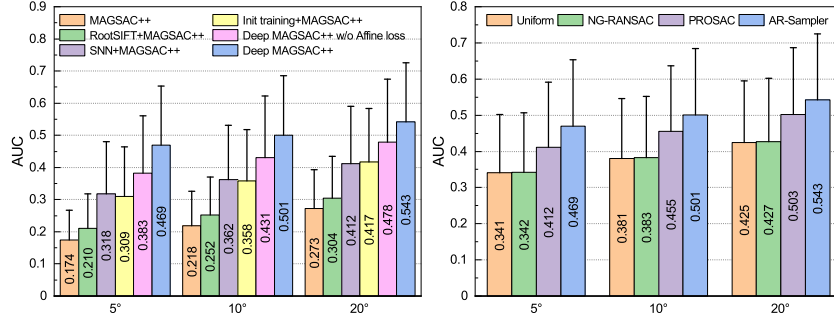


Fig. 4. The AUC scores (and their std.) at 5°, 10° and 20° of \mathbf{E} estimation on the PhotoTourism dataset [42]. *Left*: the impact of each component of Deep MAGSAC++. *Right*: results using the Uniform [16], NG-RANSAC sampler [13], PROSAC [14] and the proposed AR-Sampler.

Threshold	OANet [52]	CLNet [53]	NG-RANSAC [13]	Deep MAGSAC++
@5°	0.38	0.41	0.38	0.47
@10°	0.44	0.48	0.43	0.50
@20°	0.51	0.56	0.49	0.54

Table 2. AUC scores [51] of essential matrix estimation using the pre-trained models provided by the authors of NG-RANSAC, OANet and CLNet. CLNet and OANet was trained on 541 184 image pairs from the YFCC [44] dataset. NG-RANSAC was trained on 10 000 pairs from scene St. Peter’s Square of PhotoTourism dataset [42]. Deep MAGSAC++ was trained on 4950 pairs.

are normalized. In contrast to essential matrix estimation, we do apply initial training as it does not improve the accuracy when estimating fundamental matrices.

Table 3 reports the run-time, the median symmetric epipolar error in pixels, the AUC and F1 scores of the estimated fundamental matrices compared to the ground truth ones. Deep MAGSAC++ leads to the highest accuracy in all metrics. Interestingly, while F1 score is only marginally higher than that of NG-RANSAC, while the AUC score is better by 5%. This implies that the F1 score is not in perfect agreement with the actual camera pose error captured in the AUC score. The run-time of Deep MAGSAC++ is the lowest, being 33% faster than NG-RANSAC. These timings exclude the prediction time which is at most 1 – 2 milliseconds. Fig. 3 shows the CDFs of the epipolar errors (middle) and the F1 scores (right) on the 9060 image pairs. Deep MAGSAC++ leads to the lowest errors and highest F1 scores.

5.3 Sampler Comparison

We test the proposed sampler on the 4950 image pairs from scene Sacre Coeur when using the standard second nearest neighbor (SNN) ratio to order the points according to the inlier probabilities. To our experiments, considering the SNN ratio directly as prior inlier probability does not lead to an improvement compared to PROSAC. However, exploiting the point ranks implied by the SNN ratio works well. Assume that we are given n points $\mathbf{p}_{i_1}, \dots, \mathbf{p}_{i_n}$ ordered by their SNN ratios s_{i_1}, \dots, s_{i_n} . Thus, $s_{i_1} \leq s_{i_2} \leq$

Method	LMEDS [38]	RSC [17]	GC-RSC [7]	MSC [10]	MSC++ [9]	EAS [15]	OANet [52]	CLNet [53]	NG-RSC [13]	Deep MAGSAC++
F1 Score (%)	38.55	56.83	66.90	57.80	60.65	55.16	64.10	64.47	69.50	69.93
AUC	0.45	0.78	0.91	0.76	0.83	0.83	0.94	0.95	0.92	0.97
Median epipolar error (px)	3.15	0.98	0.42	0.84	0.75	0.88	0.57	0.54	0.41	0.29
Time (ms)	20	32	56	233	413	310	17	13	18	12

Table 3. The F1 score, AUC score at 10° , and median symmetric epipolar error (in pixels) of fundamental matrix estimation on 9690 images pairs from the KITTI benchmark [18].

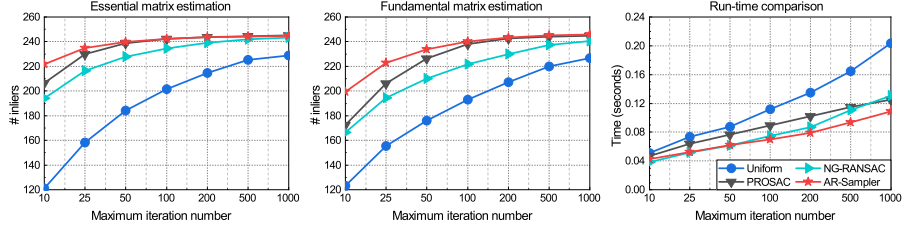


Fig. 5. *Left, middle*: the inlier numbers (vertical axis) plotted as a function of the maximum iteration number (horizontal) used in the original MAGSAC++ algorithm [9] when combined with Uniform [16], NG-RANSAC [13], PROSAC [14] and the proposed AR-Sampler. *Right*: the robust estimation time, in seconds, versus the maximum iteration number. The SNN ratio [25] provides the inlier probabilities here, without using any learning algorithms.

$\dots \leq s_{i_n}$. We calculate the prior probability of the i_j th point as $\mu_{i_j} = 1 - (j - 1)/(n - 1)$, $j \in [1, n]$. Consequently, the first point, when ordered by the SNN ratio, has 1 as prior probability. Conversely, the last one is assigned to zero.

The inlier numbers and run-times of the original MAGSAC++ when used together with the uniform [16], PROSAC [14], NG-RANSAC samplers [13], and the proposed one are shown in Fig. 5. The horizontal axis is the maximum iteration number which is a strict upper bound on the iteration number that is controlled by the RANSAC confidence parameter. The curve of the proposed sampler starts from a higher inlier number, both for essential and fundamental estimation, than that of the others, *i.e.*, it leads to finding good samples earlier than the other methods. As expected, after many iterations, all methods converge to the similar results. Due to being extremely efficient, AR-Sampler leads to the fastest robust estimation, as shown in the right plot of Fig. 5.

6 Conclusion

In this paper, we propose the Deep MAGSAC++ algorithm that achieves state-of-the-art accuracy while having comparable or better processing time to its less accurate alternatives. It runs in *real-time* on most of the tested problems. Moreover, we show that exploiting additional geometric information (*e.g.*, SIFT orientations and scales) in the loss function helps in capturing the underlying scene geometry. This extra information is available *for free* when using partially affine covariant feature detectors, *e.g.*, SIFT. The proposed AR-Sampler is superior to the traditional ones both when using

predicted weights or SNN ratios as inlier probabilities. It is also demonstrated that the proposed Deep MAGSAC++ generalizes better than the state-of-the-art learning-based approaches and is able to learn the underlying scene geometry better thanks to the number of proposed improvements. We will make the source code and the models public.

References

1. Ransac tutorial 2020- data. <https://github.com/ducha-aiki/ransac-tutorial-2020-data>
2. Arandjelović, R., Zisserman, A.: Three things everyone should know to improve object retrieval. In: 2012 IEEE Conference on Computer Vision and Pattern Recognition (CVPR). pp. 2911–2918. IEEE (2012)
3. Barath, D., Chin, T.J., Chum, O., Mishkin, D., Ranftl, R., Matas, J.: RANSAC in 2020 tutorial. In: Proceedings of the IEEE Conference on Computer Vision and Pattern Recognition (CVPR) (2020), <http://cmp.felk.cvut.cz/cvpr2020-ransac-tutorial/>
4. Barath, D.: Five-point fundamental matrix estimation for uncalibrated cameras. In: Proceedings of the IEEE Conference on Computer Vision and Pattern Recognition (CVPR). pp. 235–243 (2018)
5. Barath, D., Hajder, L.: Efficient recovery of essential matrix from two affine correspondences. *IEEE Transactions on Image Processing* **27**(11), 5328–5337 (2018)
6. Barath, D., Kukelova, Z.: Homography from two orientation-and scale-covariant features. In: The IEEE International Conference on Computer Vision (ICCV). pp. 1091–1099 (2019)
7. Barath, D., Matas, J.: Graph-cut RANSAC. In: Proceedings of the IEEE Conference on Computer Vision and Pattern Recognition (CVPR). pp. 6733–6741 (2018)
8. Barath, D., Matas, J.: Progressive-X: Efficient, anytime, multi-model fitting algorithm. In: The IEEE International Conference on Computer Vision (ICCV). pp. 3780–3788 (2019)
9. Barath, D., Neskova, J., Ivashechkin, M., Matas, J.: Magsac++, a fast, reliable and accurate robust estimator. In: Proceedings of the IEEE Conference on Computer Vision and Pattern Recognition (CVPR). pp. 1304–1312 (2020)
10. Barath, D., Neskova, J., Matas, J.: MAGSAC: marginalizing sample consensus. In: Proceedings of the IEEE Conference on Computer Vision and Pattern Recognition (CVPR) (2019), <https://github.com/danini/magsac>
11. Barath, D., Neskova, J., Matas, J.: Marginalizing sample consensus. *IEEE Transactions on Pattern Analysis and Machine Intelligence* (2021)
12. Bay, H., Tuytelaars, T., Van Gool, L.: SURF: Speeded up robust features. In: The European Conference on Computer Vision (ECCV). pp. 404–417. Springer (2006)
13. Brachmann, E., Rother, C.: Neural-guided ransac: Learning where to sample model hypotheses. In: The IEEE International Conference on Computer Vision (ICCV). pp. 4322–4331 (2019)
14. Chum, O., Matas, J.: Matching with PROSAC-progressive sample consensus. In: Proceedings of the IEEE Conference on Computer Vision and Pattern Recognition (CVPR). IEEE (2005)
15. Fan, A., Ma, J., Jiang, X., Ling, H.: Efficient deterministic search with robust loss functions for geometric model fitting. *IEEE Transactions on Pattern Analysis and Machine Intelligence* (2021)
16. Fischler, M.A., Bolles, R.C.: Random sample consensus: a paradigm for model fitting with applications to image analysis and automated cartography. *Communications of the ACM* (1981)

17. Fischler, M.A., Bolles, R.C.: Random sample consensus: A paradigm for model fitting with applications to image analysis and automated cartography. *Commun. ACM* **24**(6), 381–395 (Jun 1981). <https://doi.org/10.1145/358669.358692>, <https://doi.org/10.1145/358669.358692>
18. Geiger, A., Lenz, P., Urtasun, R.: Are we ready for autonomous driving? the KITTI vision benchmark suite. In: *Proceedings of the IEEE Conference on Computer Vision and Pattern Recognition (CVPR)*. IEEE (2012)
19. Ghosh, D., Kaabouch, N.: A survey on image mosaicking techniques. *Journal of Visual Communication and Image Representation* (2016)
20. Hartley, R., Zisserman, A.: *Multiple view geometry in computer vision*. Cambridge university press (2003)
21. He, K., Zhang, X., Ren, S., Sun, J.: Delving deep into rectifiers: Surpassing human-level performance on imagenet classification. In: *The IEEE International Conference on Computer Vision (ICCV)*. pp. 1026–1034 (2015)
22. Ioffe, S., Szegedy, C.: Batch normalization: Accelerating deep network training by reducing internal covariate shift. In: *Proceedings of the 32nd International Conference on Machine Learning. Proceedings of Machine Learning Research*, vol. 37, pp. 448–456. PMLR, Lille, France (07–09 Jul 2015), <https://proceedings.mlr.press/v37/ioffe15.html>
23. Isack, H., Boykov, Y.: Energy-based geometric multi-model fitting. *International Journal of Computer Vision (IJCV)* (2012)
24. Kingma, D.P., Ba, J.: Adam: A method for stochastic optimization. *arXiv preprint arXiv:1412.6980* (2014)
25. Lowe, D.G.: Object recognition from local scale-invariant features. In: *The IEEE International Conference on Computer Vision (ICCV)*. IEEE (1999)
26. Ma, J., Jiang, X., Fan, A., Jiang, J., Yan, J.: Image matching from handcrafted to deep features: A survey. *International Journal of Computer Vision (IJCV)* **129**(1), 23–79 (2021)
27. Maronna, R.A., Martin, R.D., Yohai, V.J., Salibián-Barrera, M.: *Robust statistics: theory and methods* (with R). John Wiley & Sons (2019)
28. Matas, J., Chum, O., Urban, M., Pajdla, T.: Robust wide-baseline stereo from maximally stable extremal regions. *IVC* (2004)
29. Mikolajczyk, K., Tuytelaars, T., Schmid, C., Zisserman, A., Matas, J., Schaffalitzky, F., Kadir, T., Van Gool, L.: A comparison of affine region detectors. *International journal of computer vision* **65**(1), 43–72 (2005)
30. Mishkin, D., Matas, J., Perdoch, M.: MODS: Fast and robust method for two-view matching. *Computer Vision and Image Understanding* **141**, 81–93 (2015)
31. Myatt, D., Torr, P., Nasuto, S., Bishop, J., Craddock, R.: NAPSAC: High noise, high dimensional robust estimation-it’s in the bag. In: *Proceedings of the British Machine Vision Conference*. pp. 44.1–44.10. BMVA Press (2002)
32. Ni, K., Jin, H., Dellaert, F.: GroupSAC: Efficient consensus in the presence of groupings. In: *The IEEE International Conference on Computer Vision (ICCV)*. pp. 2193–2200. IEEE (2009)
33. Pham, T.T., Chin, T.J., Schindler, K., Suter, D.: Interacting geometric priors for robust multimodel fitting. *IEEE Transactions on Image Processing* **23**(10), 4601–4610 (2014)
34. Pritchett, P., Zisserman, A.: Wide baseline stereo matching. In: *The IEEE International Conference on Computer Vision (ICCV)*. IEEE (1998)
35. Ranftl, R., Koltun, V.: Deep fundamental matrix estimation. In: *The European Conference on Computer Vision (ECCV)* (2018)
36. Raposo, C., Barreto, J.P.: Theory and practice of structure-from-motion using affine correspondences. In: *Proceedings of the IEEE Conference on Computer Vision and Pattern Recognition (CVPR)*. pp. 5470–5478 (2016)

37. Rousseeuw, P.J.: Least median of squares regression. *Journal of the American statistical association* **79**(388), 871–880 (1984)
38. Rousseeuw, P.J., Leroy, A.M.: *Robust regression and outlier detection*, vol. 589. John Wiley & sons (2005)
39. Rublee, E., Rabaud, V., Konolige, K., Bradski, G.: ORB: An efficient alternative to SIFT or SURF. In: 2011 International Conference on Computer Vision (ICCV). pp. 2564–2571. Ieee (2011)
40. Schönberger, J.L., Frahm, J.M.: Structure-from-motion revisited. In: *Proceedings of the IEEE Conference on Computer Vision and Pattern Recognition (CVPR)* (2016)
41. Schönberger, J.L., Zheng, E., Pollefeys, M., Frahm, J.M.: Pixelwise view selection for unstructured multi-view stereo. In: *The European Conference on Computer Vision (ECCV)* (2016)
42. Snavely, N., Seitz, S.M., Szeliski, R.: Photo tourism: exploring photo collections in 3d. In: *ACM siggraph 2006 papers*, pp. 835–846. Association for Computing Machinery, New York, NY, United States (2006)
43. Sun, W., Jiang, W., Tagliasacchi, A., Trulls, E., Yi, K.M.: Attentive context normalization for robust permutation-equivariant learning. In: *Proceedings of the IEEE Conference on Computer Vision and Pattern Recognition (CVPR)* (2020)
44. Thomee, B., Shamma, D.A., Friedland, G., Elizalde, B., Ni, K., Poland, D., Borth, D., Li, L.J.: Yfcc100m: The new data in multimedia research. *Communications of the ACM* **59**(2), 64–73 (2016)
45. Torr, P.H.S., Murray, D.W.: Outlier detection and motion segmentation. In: *Optical Tools for Manufacturing and Advanced Automation*. International Society for Optics and Photonics (1993)
46. Torr, P.H.S., Zisserman, A.: MLESAC: A new robust estimator with application to estimating image geometry. *Computer Vision and Image Understanding (CVIU)* (2000)
47. Torr, P.H.S., Zisserman, A., Maybank, S.J.: Robust detection of degenerate configurations while estimating the fundamental matrix. *Computer Vision and Image Understanding (CVIU)* (1998)
48. Ulyanov, D., Vedaldi, A., Lempitsky, V.: Instance normalization: The missing ingredient for fast stylization. *arXiv preprint arXiv:1607.08022* (2016)
49. Van Erven, T., Harremos, P.: Rényi divergence and kullback-leibler divergence. *IEEE Transactions on Information Theory* **60**(7), 3797–3820 (2014)
50. Yi*, K.M., Trulls*, E., Ono, Y., Lepetit, V., Salzmann, M., Fua, P.: Learning to find good correspondences. In: *Proceedings of the IEEE Conference on Computer Vision and Pattern Recognition (CVPR)* (2018)
51. Yi, K.M., Trulls, E., Ono, Y., Lepetit, V., Salzmann, M., Fua, P.: Learning to find good correspondences. In: *Proceedings of the IEEE Conference on Computer Vision and Pattern Recognition (CVPR)*. pp. 2666–2674 (2018)
52. Zhang, J., Sun, D., Luo, Z., Yao, A., Zhou, L., Shen, T., Chen, Y., Quan, L., Liao, H.: Learning two-view correspondences and geometry using order-aware network. *The IEEE International Conference on Computer Vision (ICCV)* (2019)
53. Zhao, C., Ge, Y., Zhu, F., Zhao, R., Li, H., Salzmann, M.: Progressive correspondence pruning by consensus learning. In: *The IEEE International Conference on Computer Vision (ICCV)* (2021)
54. Zuliani, M., Kenney, C.S., Manjunath, B.S.: The multiRANSAC algorithm and its application to detect planar homographies. In: *IEEE International Conference in Image Processing (ICIP)*. IEEE (2005)